

# Ultrahigh-Energy Gamma-ray Emission Associated with Black Hole-Jet Systems

LHAASO Collaboration

Black holes (BH), one of the most intriguing objects in the universe, can manifest themselves through electromagnetic radiations initiated by the accretion flow<sup>1</sup>. Some stellar-mass BHs drive relativistic jets when accreting matter from their companion stars, called microquasars<sup>3</sup>. Non-thermal emission from the radio to tera-electronvolt (TeV) gamma-ray band has been observed from microquasars, indicating acceleration of relativistic particles by the system<sup>4-7</sup>. Here we report detection of ultrahigh-energy (UHE, photon energy  $E > 100$  TeV) gamma-ray associated with 5 out of 12 microquasars harboring BHs visible by the Large High Altitude Air Shower Observatory, namely, SS 433, V4641 Sgr, GRS 1915+105, MAXI J1820+070, and Cygnus X-1. In the central region of SS 433, extended UHE emission is detected in spatial coincidence with a giant gas cloud, suggesting the hadronic origin of the emission. An elongated source is discovered from V4641 Sgr with the spectrum continuing up to 800 TeV. GRS 1915+105, MAXI J1820+070 and Cygnus X-1 are detected with quasi-stable radiations up to  $\sim 100$  TeV. The detection of UHE gamma-rays demonstrates that accreting BHs and their environments can operate as extremely efficient accelerators of particles out of 1 peta-electronvolt (PeV), thus contributing to Galactic cosmic rays especially around the ‘knee’ region.

The accretion process of BHs may lead to various vibrant astrophysical phenomena over a wide range of radiation bands through converting the gravitational energy of falling matters or rotational energy of BHs into energetic particles. Presence of powerful jets is tightly correlated with the accretion state and may usually be an indication of high accretion rate and efficient extraction of BH’s rotational energy<sup>8,9</sup>. Accreting BHs have long been suggested as efficient accelerators of particles exceeding 100 TeV<sup>10-12</sup>, but it is not clear how much is their contribution to the measured cosmic ray (CR) flux. Gamma-ray emissions are usually considered as an effective probe of energetic particle acceleration processes. While UHE photons from activities of accreting supermassive BHs in the distant universe (i.e., active galactic nuclei, AGN) cannot be detected due to severe absorption by the extragalactic background light and the cosmic microwave background (CMB) permeating the universe, Galactic microquasars provide us with an opportunity to look closely into the acceleration of high-energy particles in BH-jet systems.

Among about dozens of BH-jet systems identified in the Milky Way thus far, only a few of them have been detected in high-energy (HE, energy above 0.1 GeV) and very-high-energy (VHE, energy above 0.1 TeV) gamma-ray bands: previous observations detected sporadic HE gamma-ray emissions<sup>13-15</sup> and hour-scale TeV flares<sup>16</sup> from Cygnus X-1; Individual HE flares were reported from V404 Cygni<sup>17-19</sup> although the validity of these results was challenged by a later independent analysis<sup>20</sup>; A tentative VHE flare was reported from GRS 1915+105<sup>21</sup>. So far, only one microquasar, SS 433, has been unambiguously detected up to a few tens of TeV energy<sup>6,7,22-25</sup>, implying acceleration of  $\sim 100$  TeV electrons.

The Large High Altitude Air Shower Observatory (LHAASO) is a mega-scale instrument

Microquasar	Distance (kpc)	LHAASO Source	Significance ( $\sigma$ )	Photon Index	Energy Range (TeV)	Extension <sup>a</sup>	Flux <sup>b</sup> (Crab Unit)
SS 433 E.		J1913+0457	9.7 <sup>c</sup>	$2.78 \pm 0.19$	25 – 100	$0.70^\circ$	0.10
SS 433 W.	$4.6 \pm 1.3^{33}$	J1910+0509	8.6 <sup>c</sup>	$2.92 \pm 0.21$	25 – 100		0.082
SS 433 central		J1911+0513	9.8	$4.03 \pm 0.29$	100 – 400	$0.32^\circ$	0.32
V4641 Sgr	$6.2 \pm 0.7^{34}$	J1819-2541	8.1	$2.67 \pm 0.27$	40 – 1000	$0.36^\circ$	3.9
GRS 1915+105	$9.4 \pm 0.6^{35}$	J1914+1049	6.1	$3.07 \pm 0.15$	25 – 400	$0.33^\circ$	0.17
MAXI J1820+070	$2.96 \pm 0.33^{36}$	J1821+0726	5.9	$3.19 \pm 0.29$	25 – 400	$< 0.28^\circ$	0.13
Cygnus X-1	$2.2 \pm 0.2^{37}$	J1957+3517	4.0	$4.07 \pm 0.35$	25 – 100	$< 0.22^\circ$	$< 0.01$
XTE J1859+226	$4.2 \pm 0.5^{38}$	–	1.9	–	–	–	$< 0.03$
GS 2000+251	$2.7 \pm 0.7^{39}$	–	1.7	–	–	–	$< 0.04$
CI Cam	$4.1_{-0.2}^{+0.340}$	–	1.4	–	–	–	$< 0.03$
GRO J0422+32	$2.49 \pm 0.3^{41}$	–	0.8	–	–	–	$< 0.01$
V404 Cygni	$2.39 \pm 0.14^{42}$	–	0.5	–	–	–	$< 0.02$
XTE J1118+480	$1.7 \pm 0.1^{43}$	–	0	–	–	–	$< 0.01$
V616 Mon	$1.06 \pm 0.1^{44}$	–	0	–	–	–	$< 0.01$

<sup>a</sup> separation between two point-like sources of SS 433 below 100 TeV; 39% containment radius for SS 433 central, V4641 Sgr and GRS 1915+105; one-tailed 95% confidence upper limit for the source size for MAXI J1820+070 and Cygnus X-1.

<sup>b</sup> at 100 TeV, 1 CrabUnit  $\simeq 10^{-12}$  erg cm<sup>-2</sup>s<sup>-1</sup>

<sup>c</sup> the combined detection significance for the two point-like sources is  $12.9\sigma$ .

Table 1: LHAASO’s measurement of Galactic BH-jet systems in the field of view.

for the gamma-ray detection over a wide energy range from 1 TeV to a few PeV. As of now, LHAASO has reached an exceptional sensitivity of  $10^{-14}$  erg cm<sup>-2</sup>s<sup>-1</sup> at approximately 100 TeV photon energy for point-like sources, making it an ideal detector for UHE gamma-ray sources that probe accelerators of CRs around and beyond PeV energies. In LHAASO’s field of view, there are twelve microquasars with dynamic evidences for BHs as central engines<sup>26–28</sup> (see Table 1). Given these objects being located within 10 kpc from the Earth, investigations in depth could be carried out by LHAASO in the UHE band, since the absorption of UHE photons is not severe within this distance.

Using the latest LHAASO dataset of photons above 25 TeV, we detect five sources at significance levels of  $12.9\sigma$ ,  $8.6\sigma$ ,  $6.1\sigma$ ,  $5.9\sigma$  and  $4.0\sigma$ , respectively, associated with SS 433, V4641 Sgr, GRS 1915+105, MAXI J1820+070 and Cygnus X-1. Except for Cygnus X-1, the maximum photon energies of all these sources well exceed 100 TeV, strongly indicating that BH-jet systems can power efficient particle accelerators. There is no gamma-ray source with significance over  $3\sigma$  identified from other seven microquasars. It is interesting to note that SS 433 and Cygnus X-1 have persistent BH activities, and V4641 Sgr, GRS 1915+105, and MAXI J1820+070 exhibited remarkable radio or X-ray outbursts<sup>29–31</sup> in recent years. On the other hand, those undetected microquasars have not shown notable outbursts for many years. Such a contrast indicates a connection between the UHE emission and activities of BHs. Our observational results are summarized in Table 1, and significance maps & spectra of the five detected sources are shown in Figure 1, Figure 2 and Figure 3

In a BH-jet system, there are several potential particle acceleration sites. Apparently, termination shocks formed by interactions between jets and the ambient medium are promising particle

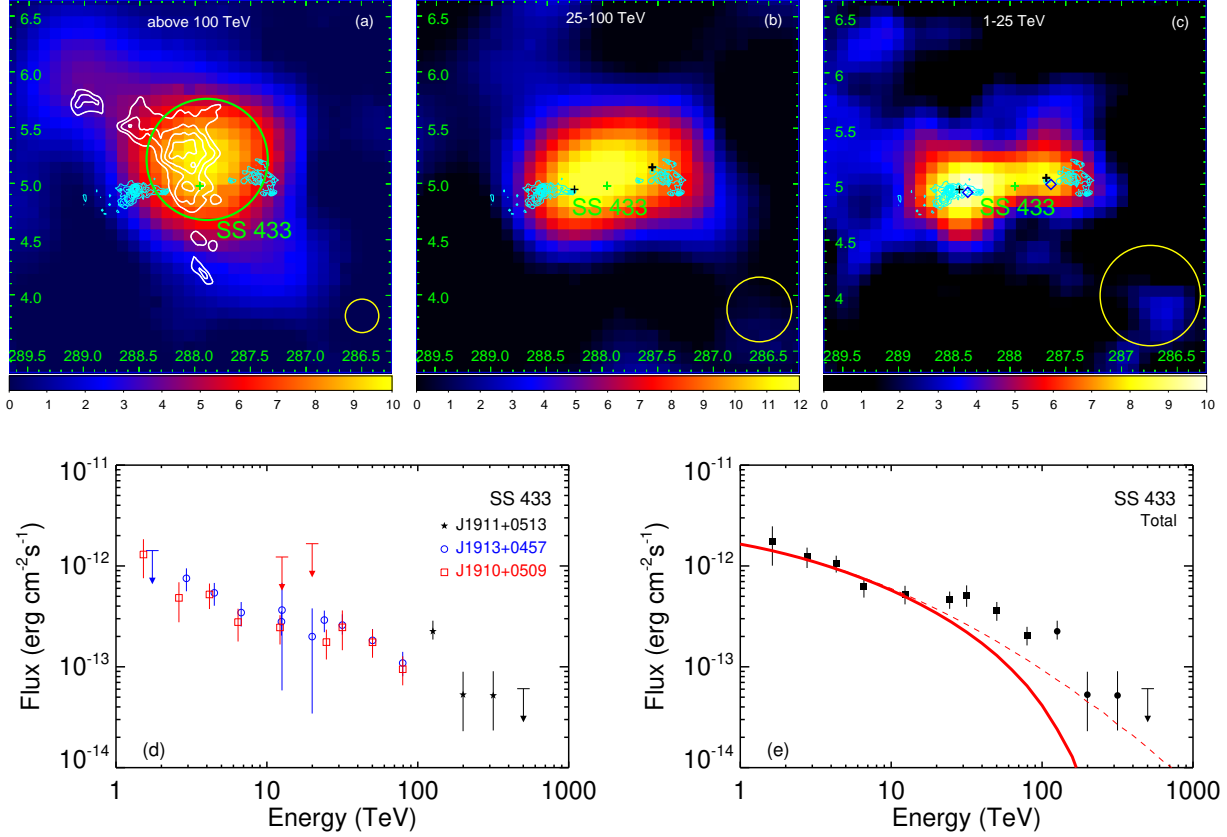


Figure 1: Significance maps and spectral energy distribution (SED) of SS 433 measured by LHAASO. Panel (a)-(c): SS 433 at energy above 100 TeV, 25-100 TeV and 1-25 TeV. In top three panels, the green cross marks the position of the BH of SS 433. In panel (a), the white contour indicates the HI atomic clouds at consistent distance of SS 433<sup>25</sup> (see Method). In panel (b) and (c), black crosses indicate the position of resolved two point-like sources at 25-100 TeV and 1-25 TeV. In panel (c), the blue diamonds shows the position of HESS detected gamma-ray emission above 10 TeV<sup>7</sup>. The cyan contour show the X-ray emission of the two lobes<sup>25</sup>. The green circle in panel (a) exhibit 68% containment radii of the LHAASO source. The yellow circles show the corresponding 68% containment radii of LHAASO PSF at the corresponding energy range. Panel (d) shows spectra of two point-like sources associated with the east and west lobes of SS 433 with blue circles red circles respectively. The spectrum of the central extended source is shown with the black stars; Panel (e) compares the total measured spectrum (with the fluxes associated with the two lobes summed up) and the prediction of a pure leptonic model for the TeV emission of the two lobes. In the modeling, relativistic electrons are injected in the form of a power-law spectrum with an index of -2.3, followed by a high-energy super-exponential cutoff at  $E_{e,\max} = 200$  TeV. The total electron injection luminosity above 1 TeV is  $L_e = 6 \times 10^{35}$  erg/s. The thick red solid curve shows the IC radiation. The thin red dashed curve shows the result assuming an extreme  $E_{e,\max} = 10$  PeV for reference. Due to the KN effect, the IC flux above  $\sim 10$  TeV is gradually suppressed and an additional spectral component is needed to explain the flux around 100 TeV. See Methods for more detailed discussions.

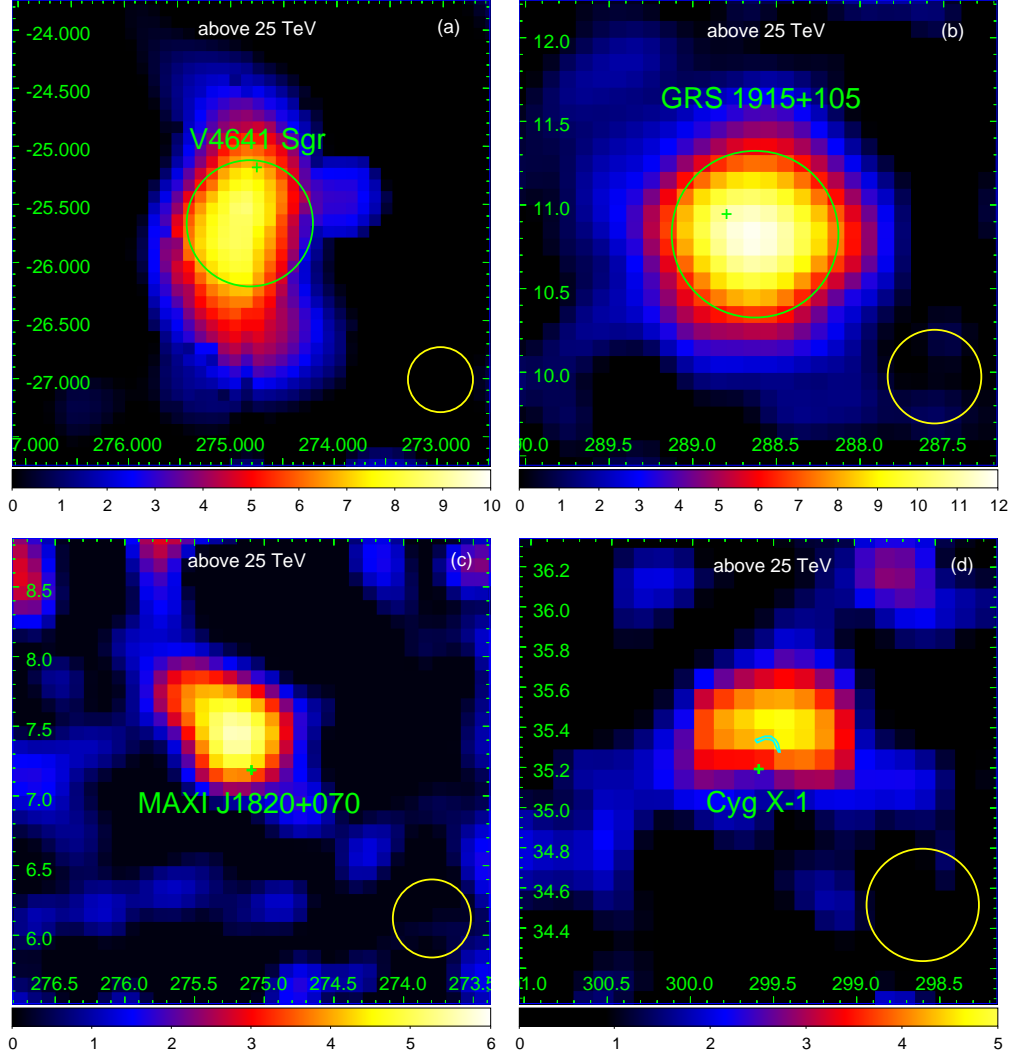


Figure 2: Significance maps of four other LHAASO measured microquasars besides SS 433. Panel (a) V4641 Sgr, (b) GRS 1915+195, (c) MAXI J1820+070 and (d) Cygnus X-1 at above 25 TeV. In each panel, the green cross marks the position of the BH of each microquasar. The green circle exhibits 68% containment radii of the LHAASO sources. The cyan arc in panel (d) represents the bow-like radio structure inflated by the jet of Cygnus X-1<sup>32</sup>. The yellow circle in each panel shows the corresponding 68% containment radii of LHAASO PSF.

accelerators, as evidenced by nonthermal radiation observed from lobes of SS 433. In addition, powerful sub-relativistic winds may be launched from the accretion disk<sup>45</sup>. Expansion of winds into the ambient medium can generate shocks and provide another potential particle acceleration site<sup>25</sup>. Particles may be also energized at the boundary between the jet and the wind, or within the jet's outer layer of stratified velocity via the shear mechanism<sup>46</sup>. Besides, particle acceleration may take place in more compact regions of the system as well. For example, internal dissipation within jets, such as internal shocks and magnetic reconnection events, is also usually considered as the efficient particle accelerator<sup>5</sup>. The fast-rotating magnetosphere of the BH offers an alternative possibility via the centrifugal force<sup>47,48</sup>. Note that particles accelerated in the compact regions may also produce extended gamma-ray sources, if these particles escape the acceleration site and diffuse to ambient media of the BHs.

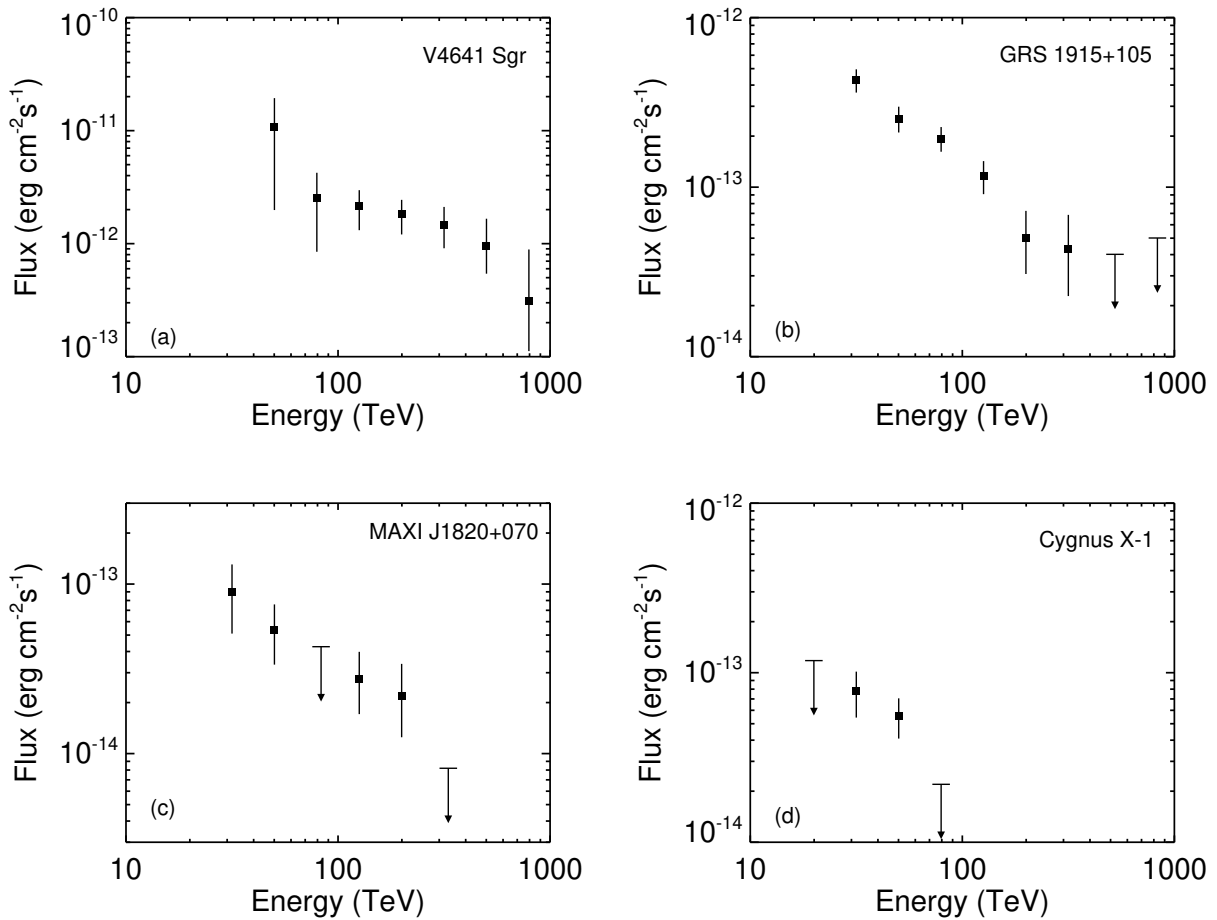


Figure 3: Spectra of the LHAASO sources associated with four microquasars. (a) V4641 Sgr; (b) GRS 1915+105; (c) MAXI J1820+070; (d) Cygnus X-1.

SS 433 is a microquasar presenting a pair of jets launched from the central BH. The two jets are nearly perpendicularly to our line of sight and terminated at approximately 40 parsecs

away from the BH. Above 100 TeV, LHAASO identified an extended source of  $9.8 \sigma$  confidence level centred at RA=  $287.89^\circ \pm 0.11^\circ$ , Dec=  $5.22^\circ \pm 0.12^\circ$ , which is  $0.25^\circ$  north of the BH. The morphology of the source, namely, LHAASO J1911+0513, is best described with a 2-dimensional Gaussian template with  $r_{39} = 0.32^\circ \pm 0.09^\circ$ . Interestingly, the source is spatially coincident with a giant atomic cloud of  $25000 M_\odot^{25}$  as shown with the white contours in Figure 1a. This supports a hadronic origin of the UHE emission of SS 433 via the proton-proton collision between accelerated protons and hydrogen nuclei in the cloud. At 25 – 100 TeV, the best description of the source morphology changes from one extended component to a structure dominated by the two point-like components (see Figure 1b) and such a morphological change becomes more evident at lower energy (see Figure 1c for 1 – 25 TeV measurement). The two point-like sources detected by LHAASO in 25 – 100 TeV, LHAASO J1913+0457 (RA=  $288.25^\circ \pm 0.03^\circ$ , Dec=  $4.95^\circ \pm 0.03^\circ$ ), and LHAASO 1910+0509 (RA=  $287.55^\circ \pm 0.04^\circ$ , Dec=  $5.15^\circ \pm 0.03^\circ$ ), are associated with the east and west lobes seen in the X-ray band respectively, and are also spatially consistent with the HESS measurement<sup>7</sup>. Such an energy-dependent morphology of SS 433 indicates a distinct origin of the emission above 100 TeV from that below 25 TeV, whereas in 25–100 TeV there may a mixed contribution from the both origins. Since HESS measurement suggests that the TeV emission of two lobes arise from inverse Compton (IC) radiation of electrons<sup>7</sup>, we perform a phenomenological fitting to total measured flux of the two point-like sources below 25 TeV with a pure leptonic model. As shown in Figure 1e, our data up to 30 TeV can be explained well via the IC radiation of electrons. However, the data at higher energies as well as that from the central extended source above 100 TeV cannot be reproduced with the same model because of the suppression by the Klein-Nishina (KN) effect. This situation entails an additional high-energy spectral component, corroborating the hadronic origin of UHE emission from the central region. A further modeling including an additional hadronic component suggests that SS 433 are continuously injecting PeV protons at a power of  $\sim 10^{38}$  erg/s into the surrounding medium (see Methods and Extended Data Figure 2 for more details). These energetic protons can be produced either close to the BH at the centre of the system, or at the two lobes (i.e., jet terminations). Deeper observations at the UHE gamma-ray band as well as those in the X-ray and radio bands are crucial in unraveling the acceleration mechanism and site of the PeV protons.

An extended sources, LHAASO J1819-2541 is discovered in the vicinity of V4641 Sgr. The centre of the source (RA=  $274.82^\circ \pm 0.09^\circ$ , DEC=  $-25.68^\circ \pm 0.11^\circ$ ) is offset from V4641 Sgr by about  $0.18^\circ$ . There is no other reasonable astrophysical counterparts of better spatial association with the LHAASO source, and therefore V4641 Sgr is the best candidate origin of LHAASO J1819-2541. The measured spectrum can be described by a power-law function with an index of -2.67. The highest energy of photons detected from this source reaches 0.8 PeV. The IC radiation of electrons cannot reproduce such a hard spectrum up to almost 1 PeV due to the KN effect, unless a very hard injection spectrum is assumed<sup>49</sup>. On the other hand, if the emission is of the hadronic origin, a more reasonable spectrum of protons can be obtained. In this case, given that the spectrum does not show a clear cutoff feature, V4641 Sgr is most likely a so-called super-PeVatron that energizes protons up to energies at least  $\sim 10$  PeV.

As the first known Galactic object ejecting matters with relativistic motion<sup>50</sup>, GRS 1915+105

is the famous archetypal microquasar. We discovered an extended source, LHAASO J1914+1049 (RA=  $288.63^\circ \pm 0.06^\circ$ , DEC=  $10.83^\circ \pm 0.06^\circ$ ), located at  $0.21^\circ$  southwest of GRS 1915+105. Similar to the situation of V4641 Sgr, there is no other potential astrophysical counterpart of this source better than GRS 1915+105, so the microquasar likely accounts for the LHAASO source. ALMA has discovered two hotspots both at  $0.28^\circ$  (corresponding to about 50 pc) away from GRS 1915+105 in the opposite directions of the BH<sup>51</sup>, which may be interpreted as two lobes. Indeed, the angular separation between the two ALMA hotspots is comparable to the extension of the LHAASO source with  $r_{39} = 0.33^\circ$ . It could be due to the large distance of GRS 1915+105 (i.e., 9.4 kpc<sup>35</sup>), so that LHAASO does not resolve their emissions. Alternatively, the extended nature of the source and the offset from the BH may be ascribed to the spatial distribution of the surrounding gas, if the emission from GRS 1915+195 is dominated by hadronic processes.

MAXI J1820+070 and Cygnus X-1 are associated with point-like sources, LHAASO J1821+0726 (RA=  $275.20^\circ \pm 0.06^\circ$ , DEC=  $7.43^\circ \pm 0.06^\circ$ ) and LHAASO J1957+3517 (RA=  $299.48^\circ \pm 0.14^\circ$ , DEC=  $35.37^\circ \pm 0.06^\circ$ ), respectively. MAXI J1820+070 was discovered in 2018 during its X-ray outburst<sup>52</sup>. A pair of bipolar relativistic radio ejecta was launched from the central black hole during the outburst<sup>31</sup>. Although the LHAASO source is detected at  $0.27^\circ$  northeast of the BH, it is in alignment with the propagation direction of the receding ejecta. There is also an offset of  $0.19^\circ$  between Cygnus X-1 and the associated LHAASO source. The offset follows the same direction of the radio-emitting bow-like structure (shown as the cyan arc in Figure 2d) that appears to be inflated by the jet launched from the central BH<sup>32</sup>. Extension of these two LHAASO sources are not evident, and in turn we obtain upper limits of  $0.28^\circ$  and  $0.22^\circ$  for the sizes of J1821+0726 and J1957+3517 respectively. While we do not expect variability of emission from extended sources, the flux of a point-like source may in principle vary with time. We therefore check their temporal behaviours, but find no evidence of variability. Future continuous observation of LHAASO is crucial for further clarification of the morphological, spectral and temporal properties of these two sources.

Detection of UHE gamma-ray emissions from these microquasars demonstrates that BH-jet systems are efficient particle accelerators. In particular, our spectral and morphological analyses of SS 433 strongly support the hadronic origin of its UHE emission, and reveal their capacity of accelerating protons to energies up to or even beyond the so-called ‘knee’ in the CR spectrum. A crucial subsequent question is that whether Galactic BH-jet systems are responsible for the origin of CRs above PeV energies. We may estimate their contribution based on our modeling of SS 433, which suggests an injection luminosity of approximately  $10^{38}$  erg/s for protons at the PeV energy. Accounting for the PeV proton production from the entire population in Milky Way by a reasonable factor of  $f_{\mu Q} = 10$  times that of SS 433, they are competent for supplying the PeV CR proton flux measured at Earth<sup>53</sup> (see Methods for more details). The acceleration mechanisms and acceleration sites in these BH-jet systems, on the other hand, have not been clearly identified based on our current observations. In principle, the particle acceleration may be processed at different scales and environments, ranging from the vicinity of BHs to endpoints of jets. Future observations with higher statistics and dedicated analyses of each microquasar, along with multiwavelength observations, can conduct more detailed spectral, morphological and temporal measurements. It

can facilitate our understanding of physical processes in BH-jet systems, and provide insights into UHECR acceleration in their more powerful cosmoscopic siblings harbouring supermassive BHs, such as radio galaxies and blazars.

## Methods

### Data Analyses

*LHAASO-KM2A* In this work we utilize the data acquired by LHAASO-KM2A 1/2 array from December 26, 2019 to November 30, 2020 (with a live time of 302 days), by the 3/4 array from December 1, 2020 to July 19, 2021 (with a live time of 219 days), and by the full array from July 20, 2021 to January 31, 2024 (with a live time of 884 days). In our previous analysis, only events with zenith angle less  $50^\circ$  are used and these data are used to observe the gamma-ray sources within the sky range of declination from  $-20^\circ$  to  $80^\circ$ , such as SS 433, GRS 1915+105, Cygnus X-3 and Cygnus X-1. The performance of LHAASO-KM2A have been studied in detail employing the Monte Carlo simulations<sup>54</sup>, and calibrated using the measurements of Crab Nebula as a standard candle<sup>55</sup>. The data quality control system and the long-term performance monitoring about the LHAASO-KM2A data can be found in<sup>56</sup>.

To extend the field of view of LHAASO-KM2A, the events with zenith angle ranging from  $50^\circ$  to  $60^\circ$  are also used in this work for the observation of the V4641 Sgr which has a minimum zenith angle of  $55^\circ$ . The energy reconstruction method is same as that presented in ref.<sup>55</sup> using the particle density at 50 m from the shower core and taking into account the zenith angle of the events. For events with energy above 100 TeV, the energy the resolution ranges from 42% to 7% at zenith angle less than  $50^\circ$  (more details see<sup>55</sup>), and the resolution will be around 60% to 40% at zenith angle ranging from  $50^\circ$  to  $60^\circ$ . To reduce the cosmic ray background, the muon content of each shower is used to reject cosmic ray showers. The rejection power of cosmic ray induced showers is better than 4000 at energies above 100 TeV and zenith angle less than  $50^\circ$  (more details see ref.<sup>55</sup>). The rejection power will decrease roughly by a factor of 10 for events at 100 TeV and zenith angle ranging from  $50^\circ$  to  $60^\circ$ , which is also energy dependent and the difference will be reduced as energy increasing. To check the pointing error of LHAASO-KM2A events with zenith angle from  $50^\circ$  to  $60^\circ$ , the Moon shadow is observed when its declination is with  $-20^\circ \sim -28^\circ$  which is similar with V4641 Sgr. This check yields a pointing error of  $-0.077^\circ \pm 0.030^\circ$  in the DEC direction and no obvious deviation in the RA direction, which is used to correct the observed position for V4641 Sgr. The flux measurement is also checked using the source 1LHAASO J1825-1337u. The flux derived using events with zenith angle from  $50^\circ$  to  $60^\circ$  is well consistent with that done using events with zenith angle less than  $50^\circ$ . This check guaranteed the flux observation on V4641 Sgr.

The pipeline of LHAASO-KM2A data analysis presented in ref.<sup>55</sup> is directly adopted in this analysis. Considering the energy resolution and statistics, one decade of energy is divided into five bins with a bin width of  $\log_{10} E = 0.2$ . The sky in celestial coordinates is divided into grids with size of  $0.1^\circ \times 0.1^\circ$  and filled with detected events according to their reconstructed arrival directions for each energy bin. The background map is estimated by the direct integration method. The significance of the source is estimated using a test statistic (TS) method variable as two times of the logarithmic likelihood ratio, i.e.,  $TS = 2\ln(\mathcal{L}_{s+b}/\mathcal{L}_b)$ , where  $\mathcal{L}_{s+b}$  is the maximum likelihood for including the source signal and background hypothesis and  $\mathcal{L}_b$  is null hypothesis. TS values

follow a chi-square distribution, and the number of degrees of freedom is equal to the difference in the number of free parameters between the assumptions. In the case of a point-like source with fixed position, which has only one free parameter (the normalization when ignoring the spectral distribution), the pretrial significance is  $\sqrt{TS}$ .

No remarkable TeV emission was identified in the vicinity of sources XTE J1859+226, GS 2000+251, CI Cam, GRO J0422+32, V404 Cygni, XTE J1118+480, and V616 Mon. In this analysis, we used a point-like source spatial template along with a power-law spectral model. The 95% flux upper limits are determined by considering the fixed position coordinates RA and Dec of these microquasars, and a constant spectral index of  $-4$ .

*LHAASO-WCDA* LHAASO-WCDA data adopted in this analysis covers from March 8, 2021 to May 31, 2024, with a total live time of 1092 days. Events with zenith angle larger than  $50^\circ$  or RMDS larger than 20 meters are not included to keep good event quality. RMDS is the root of mean distance square of the top 10 hottest detector units which represents the compactness of lateral distribution of air showers. The number of fired detector units,  $N_{\text{hit}}$ , is selected as the estimator of primary energy. The events are divided into six segments with  $N_{\text{hit}}$  value of [60-100), [100-200), [200-300), [300-500), [500-800) and [800-2000]. The direct integral method is adopted to estimate the cosmic ray background. With source spectrum model assumed as a simple power-law and spatial model as Gaussian extension, an iteration process based on multi-dimensional maximum likelihood is performed to derive the spectrum, position and extension. The iteration process adds one source at a time to the fitting as long as the TS of N+1 sources is greater than that of N sources by more than 25. The dust column density measured by PLANCK is introduced as the spatial template of diffuse Galactic gamma-ray emission.

LHAASO-WCDA data analysis has been carried out for sources in Table 1. Currently, WCDA only sees significant gamma-ray emission associated to SS 433 among all 12 microquasars listed in Table 1. In 1 – 25 TeV, two point-like sources was detected in SS 433 region at RA=  $288.45^\circ \pm 0.04^\circ$ , DEC=  $4.95^\circ \pm 0.03^\circ$  and RA=  $287.68^\circ \pm 0.04^\circ$ , DEC=  $5.06^\circ \pm 0.03^\circ$  with significance of  $9.8\sigma$  and  $8.3\sigma$ , which are associated with the east and west lobes, respectively (Figure 1, panel c). The spectra of the two sources could be well described by simple power laws with a index of  $2.44 \pm 0.14$  and  $2.53 \pm 0.16$ .

### **Detailed analyses of SS 433**

Given a high statistics of our data in the SS 433 region, a more detailed analysis of this region is available, including both data analysis and theoretical modeling.

*Energy dependent morphology analysis of SS 433.* The gamma-ray emission of SS 433 region at different energy ranges (1 – 25 TeV, 25 – 100 TeV and above 100 TeV) was modeled adopting one 2D Gaussian model and two-point source model with positions fixed at HESS emission above 10 TeV<sup>7</sup>, respectively. The Akaike Information Criterion (AIC) was adopted to compare the fitting of above two models and the results are shown in Extended Data Table 1. Below 100 TeV, the two-

point source model yields significant better fits over the 2D Gaussian model. At above 100 TeV, the 2D Gaussian model provide a significant better fit than two-point source model. The energy dependent morphology of SS 433 indicates different origins of the gamma-ray emission below and above 100 TeV. According to our theoretical interpretation of SS 433 (Extended Data Figure 2), both the hadronic and leptonic components may contribute to the emission in 25 – 100 TeV. We explored this scenario by fitting the 25-100 TeV data with the two-point source plus a 2D Gaussian model. The position and extension of 2D Gaussian was fixed to fitted values above 100 TeV. Comparing to the template composed of LHAASO J1913+0457 and LHAASO 1910+0509, the template including two-point source plus a 2D Gaussian model yields a comparable good fit to the data and a  $\Delta\text{AIC}$  of 1.37. However, because of limited statistics, the model parameters could not be very well constrained. Future observations may resolve the morphology in this energy range better.

*Neutral atomic gas analysis around SS 433.* The neutral atomic gas included here are the same presented in ref<sup>25</sup>. The Galactic ALFA HI (GALFA<sup>57,58</sup>) survey data from the Arecibo Observatory 305 m-telescope was investigated. These data were first used in the report by ref<sup>59</sup>. The GALFA HI cube data has a grid spacing of 1 arcmin and a velocity channel separation of 0.184 km s<sup>-1</sup>. Typical noise levels are 0.1 K rms of brightness temperature in an integrated velocity of 1 km s<sup>-1</sup>. Based on the Arecibo 21 cm HI data, we found an atomic gas excess at  $V_{LSR} \sim 66$  km/s, which corresponds to a distance of  $\sim 4.1 \pm 0.7$  kpc, consistent with that of SS 433<sup>33</sup>. The atomic gas excess is coincident with the gamma-ray emission above 100 TeV (see Extended Data Figure 1). The enhancement is located at R.A. = 288.11°, decl.= 5.31° with a radius of 15 arcmin ( $\sim 20$  pc at 4.6 kpc). The HI intensity of the main structure is  $\sim 1000$  K km s<sup>-1</sup>, indicating a total mass of  $\sim 25000M_{\odot}$ . The volume-averaged density of the HI gas enhancement is estimated to be roughly  $n_{\text{H}} = 30 \text{ cm}^{-3}$ , assuming a spherical cloud with radius  $R_c = 20$  pc.

*Phenomenological fitting to the spectrum of SS 433.* According to the energy-dependent morphology of the TeV emission associated with SS433, we envisage a scenario that the emission below a few times 10 TeV is dominated by electrons accelerated at jet terminations and emission above the energy mainly arises from hadronic interactions between protons and the atomic cloud in proximity of the central BH.

To model the IC radiation of electrons, we consider that electrons are injected with a power-law spectrum followed by a high-energy cutoff at  $E_{e,\text{max}}$ , i.e.,

$$Q_e(E_e) \equiv \frac{dN}{dE_e dt} = Q_{0,e} E_e^{-s_e} \exp(-E_e^2/E_{e,\text{max}}^2) \quad (1)$$

where  $Q_{0,e}$  is the normalisation factor. We consider cooling of injected electrons at the magnetic field of the lobes, which we fix at 20  $\mu\text{G}$  according to previous studies<sup>6,7</sup>, and the interstellar radiation field<sup>60</sup> including the CMB. As a result, the quasi-steady state of the electron spectrum, based on which we calculate the IC radiation, can be given by  $N_e(E_e) \approx Q_e(E_e) \cdot \min[t_{\text{cool}}, t_{\text{age}}]$ , where  $t_{\text{cool}}$  is the radiative cooling timescale and  $t_{\text{age}}$  is the age of the system which is generally estimated to be between 10 kyr and 100 kyr<sup>61-63</sup>. In fact, for radiation in the energy range of interest (i.e, above 1 TeV), whether  $t_{\text{age}} = 10$  kyr or 100 kyr does not make any difference.

To model the hadronic emission, we assume protons are constantly injected at the position of the microquasar with a spectrum

$$Q_p(E_p) = Q_{0,p} E_p^{-s_p} \exp(-E_p/E_{p,\max}), \quad (2)$$

where  $Q_{0,p}$  is a normalisation factor and its relation to the total proton luminosity can be given by  $L_p = \int_{1 \text{ GeV}} E_p Q_p(E_p) dE_p$ . We then can calculate the diffusion of protons in the surrounding medium and obtain the spatial distribution. We locate a spherical atomic cloud of  $25000 M_\odot$  with a radius  $R_c = 20 \text{ pc}$  at a distance of  $r_c$  from the microquasar, according to the analysis shown above. For simplicity, we assume a homogeneous gas density within the cloud. Note that the distance  $r_c$  can be larger than the projection distance in the sky, so it is considered as a free parameter with a lower limit of  $30 \text{ pc}$  (roughly the projection distance) in the modeling. With this setup, we calculate the gamma-ray flux generated in the proton-proton collision between propagated protons and the cloud following a semi-analytical method developed in the previous literature<sup>64</sup>. Since the emission of SS 433 below a few tens of TeV is dominated by the leptonic radiation, the hadronic flux need be diminished at low energies. It implies that protons of energy  $\lesssim 100 \text{ TeV}$  probably have not diffused to the cloud. More technically, the typical diffusion length (i.e.,  $\sqrt{4Dt_{\text{age}}}$  with  $D$  being the diffusion coefficient) of  $100 \text{ TeV}$  protons need be smaller than  $r_c$ , leading to a constraint  $D(100\text{TeV}) \lesssim 4 \times 10^{28} (r_c/100 \text{ pc})^2 (t_{\text{age}}/20 \text{ kyr})^{-1} \text{ cm}^2/\text{s}$ .

As shown in Figure 1e, a pure leptonic component with  $s_e = 2.3$  and  $E_{e,\max} = 200 \text{ TeV}$  (or even with  $E_{e,\max} = 10 \text{ PeV}$ ) cannot explain the observed flux above  $30 \text{ TeV}$  well. For the lepto-hadronic scenario considered here, we obtained a satisfactory fitting to the total emission of SS 433 measured by LHAASO with  $s_e = 2.4$ ,  $E_{e,\max} = 200 \text{ TeV}$ ,  $s_p = 1.8$ ,  $E_{p,\max} = 1 \text{ PeV}$ , as shown in Extended Data Figure 2a. Assuming  $r_c = 100 \text{ pc}$  and  $t_{\text{age}} = 20 \text{ kyr}$ , the diffusion coefficient is found to be  $D(E_p) \simeq 10^{28} (E_p/100 \text{ TeV})^{1/2} \text{ cm}^2/\text{s}$ . This value is much smaller than the average diffusion coefficient of the ISM, but such a condition is also found around other powerful CR sources such as our previous findings in the Cygnus X region<sup>65</sup>. The required electron luminosity above  $1 \text{ TeV}$  is  $L_e(> 1 \text{ TeV}) \simeq 6 \times 10^{35} \text{ erg/s}$  (similar to the pure leptonic scenario shown in Figure 1e), and the total proton luminosity above  $1 \text{ GeV}$  is  $L_p \simeq 10^{39} \text{ erg/s}$ . The kinetic powers of both two jets and the outflow of SS 433<sup>45,66,67</sup> exceed  $\gtrsim 10^{39} \text{ erg/s}$ , and hence the envisaged scenario is feasible from the perspective of the energy budget. Note that employed model parameters are not exclusive in this envisage picture. For example, we may also fit the SED data by locating the cloud closer to the accelerator (a smaller  $r_c$ ), assuming a slower diffusion coefficient of particles (a smaller  $D$ ), and correspondingly reducing the proton luminosity (a lower  $L_p$ ), or vice versa.

If we put aside the morphology of the source for the moment and just consider the spectral fitting, a pure hadronic model may work as well. In the simplest case, we assume a proton component of steady-state spectrum

$$N_p = N_{0,p} E_p^{-s_p} \exp(-E_p/E_{p,\max}) \quad (3)$$

interacting with target gas of density  $n_H = 10 \text{ cm}^{-3}$ . We find that the spectrum of SS 433 can be reproduced with  $s_p = 2.5$  and  $E_{p,\max} = 3 \text{ PeV}$  (see Extended Data Figure 2b). The total proton

energy above 1 GeV is  $W_p = 5 \times 10^{50} (n_H/10 \text{ cm}^{-3})^{-1}$  erg. Assuming an age of 20 kyr of the system and a constant injection rate of protons, we may obtain the proton luminosity to be  $8 \times 10^{38}$  erg/s above 1 GeV, which is energetically reasonable. Note that if the proton spectrum has a low-energy break/cutoff below certain energy (e.g., 1 TeV), the required energy will be much reduced.

### PeV CRs from the entire Population of Microquasars harboring BHs

We use the PeV proton luminosity obtained from the lepto-hadronic scenario for SS 433 as a representative value. Given the total proton luminosity to be  $10^{39}$  erg/s and a spectral slope of -1.8, we may estimate the PeV proton luminosity of SS 433 to be  $\sim 10^{38}$  erg/s. Theoretically, the total number of BH X-ray binaries in Milky Way is expected to be about 1000, with a dozen of them probably boasting an X-ray luminosity exceeding  $10^{39} \text{ erg s}^{-1}$ , which is comparable to that of SS 433. If the relativistic proton luminosity scales with the X-ray luminosity of microquasars to certain extent, it is reasonable to expect that the total proton injection luminosity from all Galactic microquasars may exceed  $\sim 10$  times that of SS 433 (i.e.,  $f_{\mu Q} \sim 10$ ).

Following the leaky box model, we may derive the PeV CR proton flux at Earth as

$$F(E_p = 1 \text{ PeV}) = \frac{c}{4\pi} \frac{L_p f_{\mu Q} t_{\text{res}}}{2\pi R_{\text{Gal}}^2 H_{\text{CR}}} \\ \approx 3 \times 10^4 \left( \frac{f_{\mu Q} L_p}{10^{39} \text{ erg s}^{-1}} \right) \left( \frac{D_{\text{ISM}}}{10^{31} \text{ cm}^2 \text{ s}^{-1}} \right)^{-1} \left( \frac{H_{\text{CR}}}{4 \text{ kpc}} \right) \left( \frac{R_{\text{Gal}}}{15 \text{ kpc}} \right)^{-2} \text{ eV cm}^{-2} \text{ s}^{-1} \text{ sr}^{-1},$$

where  $t_{\text{res}} = H_{\text{CR}}^2/4D_{\text{ISM}}$  determines the PeV CR residence time within the Galaxy with  $H_{\text{CR}}$  being the scale height of the CR halo and  $D_{\text{ISM}}$  being the average diffusion coefficient of the ISM, and  $R_{\text{Gal}}$  is the typical radius of the Galaxy. The inferred PeV proton flux is consistent with the measurement<sup>53</sup>. A recent study<sup>69</sup> argues that the distribution of PeV CRs in the ISM may be clumpy and variable because of the rarity of the sources. According to the simulation shown in the study, the observed PeV CR flux at Earth may be explained with a lower luminosity of  $L_p \approx 10^{38}$  erg/s. With these simple estimations, we see that Galactic BH-jet systems can be potentially important factories of CRs around and above the knee.

### Acknowledgement

We would like to thank all staff members who work at the LHAASO site above 4400 meter above the sea level year round to maintain the detector and keep the water recycling system, electricity power supply and other components of the experiment operating smoothly. We are grateful to Chengdu Management Committee of Tianfu New Area for the constant financial support for research with LHAASO data. We appreciate the computing and data service support provided by the National High Energy Physics Data Center for the data analysis in this paper. This research work is supported by the following grants: The National Natural Science Foundation of China No.12393851, No.12393852, No.12393853, No.12393854, No.12333006, No.12273038, No.12205314, No.12105301, No.12305120, No.12261160362, No.12105294, No.U1931201, No.12375107, No.12173039, the Department of Science and Technology of Sichuan Province, China No.24NSFSC2319,

Project for Young Scientists in Basic Research of Chinese Academy of Sciences No.YSBR-061, and in Thailand by the National Science and Technology Development Agency (NSTDA) and the National Research Council of Thailand (NRCT) under the High-Potential Research Team Grant Program (N42A650868).

### Author Contributions Statement

Z. Cao initiated the project. R.Y. Liu and J. Li led the writing of the paper. Y.H. Yu, J. Li, R.Z. Yang and S.C. Hu analysed the data of the SS 433. S.Z. Chen analysed the data of V4641 Sgr. K. Wang analysed the data of GRS 1915+105, MAXI J1820+070, and seven undetected microquasars. C. Li analysed the data of Cygnus X-1. S.Q. Xi did the cross check of the LHAASO data analyses. J. Li analysed H I data around SS 433. R.Y. Liu led the interpretation of the data. F. Aharonian and H. Feng provided important comments on the manuscript. All the authors discussed and edited the manuscript.

### Competing Interests Statement

The authors declare no competing interests.

### Correspondence

R.Y. Liu (ryliu@nju.edu.cn); J. Li (jianli@ustc.edu.cn); R.Z. Yang (yangrz@ustc.edu.cn); K. Wang(k-wang@smail.nju.edu.cn); Y.H. Yu (yuyh@ustc.edu.cn); S.Z. Chen (chensz@ihep.ac.cn); S.C. Hu (hushicong@ihep.ac.cn)

### Reference

1. Remillard, R. A. & McClintock, J. E. X-Ray Properties of Black-Hole Binaries. *Annu. Rev. Astron. Astrophys.* **44**, 49–92 (2006). [astro-ph/0606352](#).
2. Kaaret, P., Feng, H. & Roberts, T. P. Ultraluminous X-Ray Sources. *Annu. Rev. Astron. Astrophys.* **55**, 303–341 (2017). [1703.10728](#).
3. Mirabel, I. F. & Rodríguez, L. F. Sources of Relativistic Jets in the Galaxy. *Annu. Rev. Astron. Astrophys.* **37**, 409–443 (1999). [astro-ph/9902062](#).
4. Bordas, P., Bosch-Ramon, V., Paredes, J. M. & Perucho, M. Non-thermal emission from microquasar/ISM interaction. *Astron. Astrophys.* **497**, 325–334 (2009). [0903.3293](#).
5. Bosch-Ramon, V. & Khangulyan, D. Understanding the Very-High Emission from Microquasars. *International Journal of Modern Physics D* **18**, 347–387 (2009). [0805.4123](#).
6. Abeysekara, A. U. *et al.* Very-high-energy particle acceleration powered by the jets of the microquasar SS 433. *Nature* **562**, 82–85 (2018).

7. H. E. S. S. Collaboration, Olivera-Nieto, L., Reville, B., Hinton, J. & Tsirou, M. Acceleration and transport of relativistic electrons in the jets of the microquasar SS 433. *Science* **383**, 402–406 (2024).
8. Blandford, R. D. & Znajek, R. L. Electromagnetic extraction of energy from Kerr black holes. *Mon. Not. R. Astron. Soc.* **179**, 433–456 (1977).
9. Fender, R. Jets from X-ray binaries. In Lewin, W. H. G. & van der Klis, M. (eds.) *Compact stellar X-ray sources*, vol. 39, 381–419 (2006).
10. Aharonian, F. A. & Atoyan, A. M. Gamma rays from galactic sources with relativistic jets. *New Astro. Rev.* **42**, 579–584 (1998).
11. Sudoh, T., Inoue, Y. & Khangulyan, D. Multiwavelength Emission from Galactic Jets: The Case of the Microquasar SS433. *Astrophys. J.* **889**, 146 (2020). 1911.00013.
12. Khangulyan, D., Bosch-Ramon, V. & Hadasch, D. Non-thermal emission from microquasar jets: The case of GRS 1915+105. *Journal of High Energy Astrophysics* **43**, 93–104 (2024).
13. Sabatini, S. *et al.* Episodic Transient Gamma-ray Emission from the Microquasar Cygnus X-1. *Astrophys. J. Lett.* **712**, L10–L15 (2010).
14. Malyshev, D., Zdziarski, A. A. & Chernyakova, M. High-energy gamma-ray emission from Cyg X-1 measured by Fermi and its theoretical implications. *Mon. Not. R. Astron. Soc.* **434**, 2380–2389 (2013).
15. Zanin, R. *et al.* Gamma rays detected from Cygnus X-1 with likely jet origin. *Astron. Astrophys.* **596**, A55 (2016).
16. Albert, J. *et al.* Very High Energy Gamma-Ray Radiation from the Stellar Mass Black Hole Binary Cygnus X-1. *Astrophys. J. Lett.* **665**, L51–L54 (2007). 0706.1505.
17. Loh, A. *et al.* High-energy gamma-ray observations of the accreting black hole V404 Cygni during its 2015 June outburst. *Mon. Not. R. Astron. Soc.* **462**, L111–L115 (2016).
18. Piano, G., Munar-Adrover, P., Verrecchia, F., Tavani, M. & Trushkin, S. A. High-energy Gamma-Ray Activity from V404 Cygni Detected by AGILE during the 2015 June Outburst. *Astrophys. J.* **839**, 84 (2017).
19. Xing, Y. & Wang, Z. Detection of the Microquasar V404 Cygni at  $\gamma$ -Rays Revisited: Short Flaring Events in Quiescence. *Astrophys. J.* **922**, 111 (2021).
20. Harvey, M., Rulten, C. B. & Chadwick, P. M. V404 Cygni with Fermi-LAT. *Mon. Not. R. Astron. Soc.* **506**, 6029–6038 (2021).
21. Aharonian, F. A. & Heinzlmann, G. The HEGRA Experiment Status and Recent Results. *Nuclear Physics B Proceedings Supplements* **60**, 193–198 (1998).

22. Bordas, P., Yang, R., Kafexhiu, E. & Aharonian, F. Detection of Persistent Gamma-Ray Emission Toward SS433/W50. *Astrophys. J. Lett.* **807**, L8 (2015). 1411.7413.
23. Sun, X.-N., Yang, R.-Z., Liu, B., Xi, S.-Q. & Wang, X.-Y. Tentative evidence of spatially extended GeV emission from SS433/W50. *Astron. Astrophys.* **626**, A113 (2019). 1904.05127.
24. Xing, Y., Wang, Z., Zhang, X., Chen, Y. & Jithesh, V. Fermi Observation of the Jets of the Microquasar SS 433. *Astrophys. J.* **872**, 25 (2019). 1811.09495.
25. Li, J. *et al.* Gamma-ray heartbeat powered by the microquasar SS 433. *Nature Astronomy* **4**, 1177–1184 (2020).
26. Crampton, D. & Hutchings, J. B. The SS 433 binary system. *Astrophys. J.* **251**, 604–610 (1981).
27. Orosz, J. A. *et al.* The Mass of the Black Hole in Cygnus X-1. *Astrophys. J.* **742**, 84 (2011).
28. Corral-Santana, J. M. *et al.* BlackCAT: A catalogue of stellar-mass black holes in X-ray transients. *Astron. Astrophys.* **587**, A61 (2016). 1510.08869.
29. Shaw, A. W. *et al.* High resolution X-ray spectroscopy of V4641 Sgr during its 2020 outburst. *Mon. Not. R. Astron. Soc.* **516**, 124–137 (2022). 2208.01732.
30. Méndez, M. *et al.* Coupling between the accreting corona and the relativistic jet in the microquasar GRS 1915+105. *Nature Astronomy* **6**, 577–583 (2022). 2203.02963.
31. Bright, J. S. *et al.* An extremely powerful long-lived superluminal ejection from the black hole MAXI J1820+070. *Nature Astronomy* **4**, 697–703 (2020). 2003.01083.
32. Gallo, E. *et al.* A dark jet dominates the power output of the stellar black hole Cygnus X-1. *Nature* **436**, 819–821 (2005). astro-ph/0508228.
33. Luri, X. *et al.* Gaia Data Release 2. Using Gaia parallaxes. *Astron. Astrophys.* **616**, A9 (2018).
34. MacDonald, R. K. D. *et al.* The Black Hole Binary V4641 Sagittarii: Activity in Quiescence and Improved Mass Determinations. *Astrophys. J.* **784**, 2 (2014).
35. Reid, M. J. & Miller-Jones, J. C. A. On the Distances to the X-Ray Binaries Cygnus X-3 and GRS 1915+105. *Astrophys. J.* **959**, 85 (2023).
36. Atri, P. *et al.* A radio parallax to the black hole X-ray binary MAXI J1820+070. *Mon. Not. R. Astron. Soc.* **493**, L81–L86 (2020). 1912.04525.
37. Miller-Jones, J. C. A. *et al.* Cygnus X-1 contains a 21-solar mass black hole—Implications for massive star winds. *Science* **371**, 1046–1049 (2021).

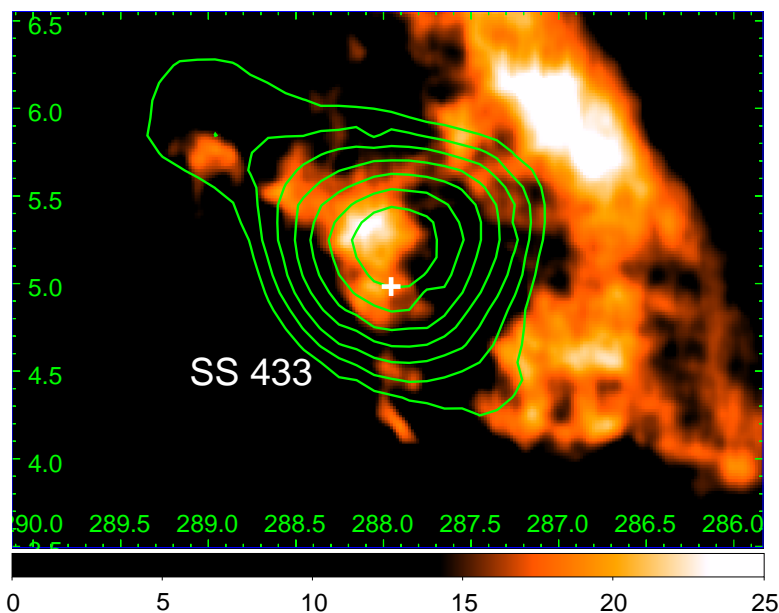
38. Shaposhnikov, N. & Titarchuk, L. Determination of Black Hole Masses in Galactic Black Hole Binaries Using Scaling of Spectral and Variability Characteristics. *Astrophys. J.* **699**, 453–468 (2009).
39. Jonker, P. G. & Nelemans, G. The distances to Galactic low-mass X-ray binaries: consequences for black hole luminosities and kicks. *Mon. Not. R. Astron. Soc.* **354**, 355–366 (2004). astro-ph/0407168.
40. Fortin, F., García, F. & Chaty, S. Finding the birthplace of HMXBs in the Galaxy using Gaia EDR3: Kinematical age determination through orbit integration. *Astron. Astrophys.* **665**, A69 (2022).
41. Gelino, D. M. & Harrison, T. E. GRO J0422+32: The Lowest Mass Black Hole? *Astrophys. J.* **599**, 1254–1259 (2003). astro-ph/0308490.
42. Miller-Jones, J. C. A. *et al.* The First Accurate Parallax Distance to a Black Hole. *Astrophys. J. Lett.* **706**, L230–L234 (2009).
43. Gelino, D. M. *et al.* The Inclination Angle and Mass of the Black Hole in XTE J1118+480. *Astrophys. J.* **642**, 438–442 (2006).
44. Cantrell, A. G. *et al.* The Inclination of the Soft X-Ray Transient A0620-00 and the Mass of its Black Hole. *Astrophys. J.* **710**, 1127–1141 (2010). 1001.0261.
45. Middleton, M. J. *et al.* NuSTAR reveals the hidden nature of SS433. *Mon. Not. R. Astron. Soc.* **506**, 1045–1058 (2021). 1810.10518.
46. Rieger, F. M. & Duffy, P. Shear Acceleration in Relativistic Astrophysical Jets. *Astrophys. J.* **617**, 155–161 (2004). astro-ph/0410269.
47. Gangadhara, R. T. & Lesch, H. On the nonthermal emission in active galactic nuclei. *Astron. Astrophys.* **323**, L45–L48 (1997). astro-ph/9707182.
48. Rieger, F. M. & Mannheim, K. Particle acceleration by rotating magnetospheres in active galactic nuclei. *Astron. Astrophys.* **353**, 473–478 (2000). astro-ph/9911082.
49. Liu, R.-Y. & Wang, X.-Y. PeV Emission of the Crab Nebula: Constraints on the Proton Content in Pulsar Wind and Implications. *Astrophys. J.* **922**, 221 (2021). 2109.14148.
50. Mirabel, I. F. & Rodríguez, L. F. A superluminal source in the Galaxy. *Nature* **371**, 46–48 (1994).
51. Tetarenko, A. J., Freeman, P., Rosolowsky, E. W., Miller-Jones, J. C. A. & Sivakoff, G. R. Mapping jet-ISM interactions in X-ray binaries with ALMA: a GRS 1915+105 case study. *Mon. Not. R. Astron. Soc.* **475**, 448–468 (2018).
52. Tucker, M. A. *et al.* ASASSN-18ey: The Rise of a New Black Hole X-Ray Binary. *Astrophys. J. Lett.* **867**, L9 (2018). 1808.07875.

53. Apel, W. D. *et al.* KASCADE-Grande measurements of energy spectra for elemental groups of cosmic rays. *Astroparticle Physics* **47**, 54–66 (2013).
54. Cao, Z. *et al.* LHAASO-KM2A detector simulation using Geant4. *Radiation Detection Technology and Methods* (2024). 2404.04801.
55. Aharonian, F. *et al.* Observation of the Crab Nebula with LHAASO-KM2A - a performance study. *Chinese Physics C* **45**, 025002 (2021).
56. Cao, Z. *et al.* Data quality control system and long-term performance monitor of the LHAASO-KM2A. *arXiv e-prints* arXiv:2405.11826 (2024). 2405.11826.
57. Peek, J. E. G. *et al.* The GALFA-HI Survey: Data Release 1. *Astrophys. J. Supp.* **194**, 20 (2011). 1101.1879.
58. Peek, J. E. G. *et al.* The GALFA-H I Survey Data Release 2. *Astrophys. J. Supp.* **234**, 2 (2018).
59. Su, Y. *et al.* The Large-scale Interstellar Medium of SS 433/W50 Revisited. *Astrophys. J.* **863**, 103 (2018). 1807.03737.
60. Popescu, C. C. *et al.* A radiation transfer model for the Milky Way: I. Radiation fields and application to high-energy astrophysics. *Mon. Not. R. Astron. Soc.* **470**, 2539–2558 (2017). 1705.06652.
61. Zealey, W. J., Dopita, M. A. & Malin, D. F. The interaction between the relativistic jets of SS433 and the interstellar medium. *Mon. Not. R. Astron. Soc.* **192**, 731–743 (1980).
62. Goodall, P. T., Alouani-Bibi, F. & Blundell, K. M. When microquasar jets and supernova collide: hydrodynamically simulating the SS 433-W 50 interaction. *Mon. Not. R. Astron. Soc.* **414**, 2838–2859 (2011). 1101.3486.
63. Han, Q. & Li, X.-D. On the Formation of SS433. *Astrophys. J.* **896**, 34 (2020). 2004.12547.
64. Kafexhiu, E., Aharonian, F., Taylor, A. M. & Vila, G. S. Parametrization of gamma-ray production cross sections for p p interactions in a broad proton energy range from the kinematic threshold to PeV energies. *Phys. Rev. D* **90**, 123014 (2014). 1406.7369.
65. LHAASO Collaboration. An ultrahigh-energy  $\gamma$ -ray bubble powered by a super pevatron. *Science Bulletin* **69**, 449–457 (2024).
66. Marshall, H. L., Canizares, C. R. & Schulz, N. S. The High-Resolution X-Ray Spectrum of SS 433 Using the Chandra HETGS. *Astrophys. J.* **564**, 941–952 (2002). astro-ph/0108206.
67. Fogantini, F. A. *et al.* A NuSTAR view of SS433. Precessional evolution of the jet-disk system. *Astron. Astrophys.* **669**, A149 (2023). 2210.09390.

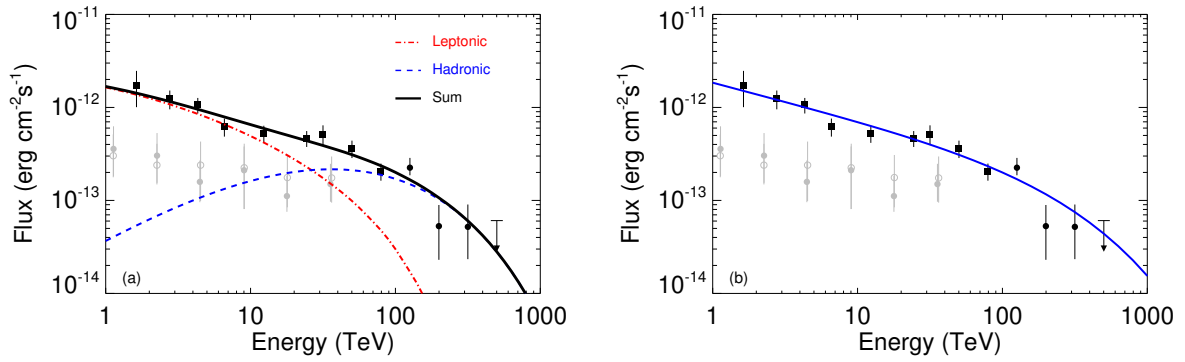
68. Shao, Y. & Li, X.-D. Population Synthesis of Black Hole X-Ray Binaries. *Astrophys. J.* **898**, 143 (2020).
69. Giacinti, G. & Semikoz, D. Model of Cosmic Ray Propagation in the Milky Way at the Knee. *arXiv e-prints* arXiv:2305.10251 (2023). 2305.10251.

	1-25 TeV	25-100 TeV	above 100 TeV
$\Delta\text{AIC}$	22.7	22.8	-12.5

Extended Data Table 1:  $\Delta\text{AIC}$  of SS 433 between 2D Gaussian model and two-point source model at different energy ranges.  $\Delta\text{AIC} < -10$  favors the 2D Gaussian model while  $\Delta\text{AIC} > -10$  favor the two-point source model.



Extended Data Figure 1: Map of the HI emission observed with Arecibo integrated in the interval  $65\text{--}82 \text{ km s}^{-1}$ . The green contours show the gamma-ray emission above 100 TeV from  $3\sigma$  with a step of  $1\sigma$ . The image has been scaled by  $\sin |b|$  ( $b$  is Galactic latitude) to enhance the features far from the Galactic plane<sup>59</sup>. The horizontal and vertical axes are R.A. and decl. in J2000.



Extended Data Figure 2: A phenomenological fitting to spectra of LHAASO sources associated with SS 433 (see Method for details of models and parameters). Panel (a): leptohadronic modeling. The thick dash-dotted red curve and thick dashed blue curve show the leptonic emission and hadronic emission respectively, while the solid black curve represent the sum of the two components. Panel (b): pure hadronic modeling. The solid blue curve shows the hadronic emission. In both two panels, black squares (below 100 TeV) and circles (above 100 TeV) represent the flux of the total emission associated with SS 433 measured by LHAASO, and the HESS measurements<sup>7</sup> of the east and the west lobes are shown with grey open and filled circles, respectively, for reference. See Methods for more details of the modeling.